



THE UNIVERSITY *of* EDINBURGH

Edinburgh Research Explorer

Gain of function DNMT3A mutations cause microcephalic dwarfism and hypermethylation of polycomb-regulated regions

Citation for published version:

Heyn, P, Logan, CV, Fluteau, A, Challis, RC, Auchynnikava, T, Martin, C-A, Marsh, JA, Taglini, F, Kilanowski, F, Parry, D, Cormier-Daire, V, Fong, C-T, Gibson, K, Hwa, V, Ibanez, L, Robertson, SP, Sebastiani, G, Rappsilber, J, Allshire, RC, Reijns, MAM, Dauber, A, Sproul, D & Jackson, AP 2019, 'Gain of function *DNMT3A* mutations cause microcephalic dwarfism and hypermethylation of polycomb-regulated regions', *Nature Genetics*, vol. 51, no. 1, pp. 96–105. <https://doi.org/10.1038/s41588-018-0274-x>

Digital Object Identifier (DOI):

[10.1038/s41588-018-0274-x](https://doi.org/10.1038/s41588-018-0274-x)

Link:

[Link to publication record in Edinburgh Research Explorer](#)

Document Version:

Peer reviewed version

Published In:

Nature Genetics

General rights

Copyright for the publications made accessible via the Edinburgh Research Explorer is retained by the author(s) and / or other copyright owners and it is a condition of accessing these publications that users recognise and abide by the legal requirements associated with these rights.

Take down policy

The University of Edinburgh has made every reasonable effort to ensure that Edinburgh Research Explorer content complies with UK legislation. If you believe that the public display of this file breaches copyright please contact openaccess@ed.ac.uk providing details, and we will remove access to the work immediately and investigate your claim.



1 **Gain of function *DNMT3A* mutations cause microcephalic dwarfism and**
2 **hypermethylation of Polycomb-regulated regions**

3

4 **Patricia Heyn¹, Clare V. Logan¹, Adeline Fluteau¹, Rachel C. Challis¹, Tatsiana**
5 **Auchynnikava², Carol-Anne Martin¹, Joseph A. Marsh¹, Francesca Taglini^{1,3},**
6 **Fiona Kilanowski¹, David A. Parry¹, Valerie Cormier-Daire⁴, Chin-To Fong⁵, Kate**
7 **Gibson⁶, Vivian Hwa⁷, Lourdes Ibáñez^{8,9}, Stephen P. Robertson¹⁰, Giorgia**
8 **Sebastiani¹¹, Juri Rappsilber^{2,12}, Robin C. Allshire², Martin A.M. Reijns¹,**
9 **Andrew Dauber^{7,13}, Duncan Sproul^{1,3*}, Andrew P. Jackson^{1*}.**

10

- 11 1. MRC Human Genetics Unit, IGMM, University of Edinburgh, Edinburgh, UK
- 12 2. Wellcome Centre for Cell Biology, School of Biological Sciences, University of
- 13 Edinburgh, Edinburgh, UK
- 14 3. Edinburgh Cancer Research Centre, IGMM, University of Edinburgh,
- 15 Edinburgh, UK
- 16 4. Department of Medical Genetics, INSERM UMR 1163, Université Paris-
- 17 Descartes-Sorbonne Paris Cité, Institut Imagine, AP-HP, Hôpital Necker-
- 18 Enfants Malades, Paris, France
- 19 5. Department of Pediatrics, University of Rochester School of Medicine and
- 20 Dentistry, Rochester, New York, USA
- 21 6. Genetic Health Service New Zealand, Christchurch Hospital, Christchurch,
- 22 New Zealand
- 23 7. Cincinnati Center for Growth Disorders, Division of Endocrinology, Cincinnati
- 24 Children's Hospital Medical Center, University of Cincinnati College of
- 25 Medicine, Cincinnati, Ohio, USA

- 26 8. Endocrinology, Pediatric Research Institute Sant Joan de Déu, University of
27 Barcelona, Barcelona, Spain
- 28 9. Centro de Investigación Biomédica en Red de Diabetes y Enfermedades
29 Metabólicas Asociadas (CIBERDEM), ISCIII, Madrid, Spain
- 30 10. Department of Women's and Children's Health, Dunedin School of Medicine,
31 University of Otago, Dunedin, New Zealand
- 32 11. Neonatology Unit, Hospital Clinic-Maternitat, ICGON, BCNatal, University of
33 Barcelona, Spain
- 34 12. Bioanalytics, Institute of Biotechnology, Technische Universität Berlin, Berlin,
35 Germany
- 36 13. Division of Endocrinology, Children's National Medical Center, Washington,
37 D.C., USA

38

39 Correspondence to:

40 Duncan.Sproul@igmm.ed.ac.uk

41 Andrew.Jackson@igmm.ed.ac.uk

42

43

44 **Abstract.**

45 DNA methylation and Polycomb are key factors in the establishment of vertebrate
46 cellular identity and fate. Here we report *de novo* missense mutations in *DNMT3A*,
47 encoding the DNA methyltransferase DNMT3A, that cause microcephalic dwarfism,
48 a hypocellular disorder of extreme global growth failure. Substitutions in the PWWP
49 domain abrogate binding to the histone modifications H3K36me2/3, and alter DNA
50 methylation in patient cells. Polycomb-associated DNA methylation canyons/valleys,
51 hypomethylated domains encompassing developmental genes, become methylated
52 with concomitant depletion of H3K27me3 and H3K4me3 bivalent marks. Such *de*
53 *nov*o DNA methylation occurs during differentiation of *Dnmt3a*^{W326R} pluripotent cells
54 *in vitro*, and is also evident in *Dnmt3a*^{W326R/+} dwarf mice. We therefore propose that
55 the interaction of the DNMT3A PWWP domain with H3K36me2/3 normally limits
56 DNA methylation of polycomb-marked regions. Our findings implicate the interplay
57 between DNA methylation and polycomb at key developmental regulators as a
58 determinant of organism size in mammals.

59

60 **Introduction**

61 Microcephalic dwarfism represents a group of conditions of profound size reduction
62 in humans. These single gene disorders are distinguished from other forms of
63 dwarfism by severity and morphology. Growth is globally impaired pre- and post-
64 natally with proportionate scaling¹. Reduced brain size in microcephalic dwarfism
65 differentiates it from other forms of dwarfism and reflects an early developmental
66 origin. We and others have discovered many microcephalic dwarfism genes to
67 encode essential components of the cell cycle machinery, including replication

68 licensing components²⁻⁵ and key mitotic proteins⁶⁻⁸. Mutations in these genes result
69 in reduced cell number and consequently organism size¹.

70

71 As cell number is also the major determinant of size differences between mammals⁹
72 and the molecular basis for many microcephalic dwarfism patients still remains to be
73 defined, we performed whole-exome sequencing (WES) to identify novel genetic
74 causes and inform understanding of size regulation.

75

76 **Results**

77 ***De novo mutations in DNMT3A causes microcephalic dwarfism***

78 WES trio analysis of a microcephalic dwarfism family identified a *de novo* *DNMT3A*
79 heterozygous mutation in the proband (NM_175629.2:c.988T>C, Fig. 1a,b and
80 Supplementary Table 1). This resulted in the replacement of a tryptophan residue
81 with an arginine at codon 330 (p.W330R) in the highly conserved PWWP domain of
82 this DNA methyltransferase (Fig. 1c). NGS sequencing of our patient cohort then
83 identified an unrelated patient with the same heterozygous *de novo* missense variant
84 in *DNMT3A* (c.988T>C p.W330R, Supplementary Table 1). This substitution was not
85 present in the GnomAD¹⁰ database suggesting it to be absent from the general
86 population. The two individuals were phenotypically similar, exhibiting significant,
87 proportionate reduction in head circumference and height (Supplementary Note,
88 clinical synopsis). The shared clinical phenotype, in conjunction with independent *de*
89 *novo* mutation of the same highly conserved residue, led us to conclude that these
90 were pathogenic mutations. More recently, we ascertained a further microcephalic
91 dwarfism patient with a *de novo* mutation in an adjacent codon (c.997G>A;
92 p.D333N). Notably, the growth parameters of all three patients contrast markedly
93 with those of previously reported patients with *de novo* germline missense and

94 truncating loss of function *DNMT3A* mutations^{11,12}, who have the reciprocal
95 phenotype of macrocephalic overgrowth Tatton-Brown Rahman syndrome (TBRS,
96 Fig. 1d). As *DNMT3A* haploinsufficiency causes overgrowth¹³, this suggested the
97 c.988T>C and c.997G>A mutations to be genetic ‘gain of function’ mutations.

98

99 ***DNMT3A^{W330R} is stably expressed***

100 To model the consequences of the W330R substitution on DNMT3A stability we
101 engineered mouse embryonic stem cells (mESCs) homozygous and heterozygous
102 for the orthologous mutation, W326R, using CRISPR/Cas9-mediated homology-
103 directed repair¹⁴. Immunoblotting of these lines established that the Dnmt3a^{W326R}
104 protein is stably expressed. In contrast, mESCs homozygous for the overgrowth
105 PWWP mutations W293del and I306N (W297del and I310N in human, respectively),
106 had markedly reduced Dnmt3a levels (Fig. 2a). We also generated recombinant
107 wildtype and mutant human DNMT3A PWWP domains as GST-fusion proteins.
108 While we were able to efficiently express and purify PWWP^{WT} and PWWP^{W330R}
109 proteins, the overgrowth PWWP^{W297del} and PWWP^{I310N} proteins did not yield stable
110 protein (Supplementary Fig. 1a). This supports the notion that the W330R mutation
111 alters PWWP function, distinct from that of PWWP overgrowth mutations, which
112 interfere with protein stability.

113

114 ***The DNMT3A^{W330R} substitution impairs binding to methylated H3K36***

115 The PWWP-domain of DNMT3A binds post-translationally modified histone H3 that
116 has been tri-methylated at Lysine 36 (H3K36me3)^{15,16}. Tryptophan 330 is one of
117 three aromatic amino acids that along with an aspartate residue (Asp333), form an
118 aromatic cage around the methylated lysine^{17,18} (Fig. 2b). Structural modelling of the

DNMT3A^{W330R} substitution predicts that the arginine substitution substantially disrupts this interaction (interaction destabilization: 11.8 kcal/mol).

To test this experimentally, we performed pulldown experiments of histone tail peptides using GST-PWWP fusion proteins. Whereas PWWP^{WT} interacted with an H3K36me3 modified histone-tail peptide but not the corresponding unmodified peptide, we did not detect an interaction of the mutant PWWP^{W330R} with H3K36me3 (Fig. 2c,d). To confirm this and assess whether the W330R substitution conferred an alternative binding specificity on the PWWP domain, a peptide array containing 384 unique and combinatorial histone tail modifications was probed with recombinant protein. PWWP^{WT} bound strongly to H3K36me3 and H3K36me2 as previously reported^{15,19}. However, under the same experimental conditions, PWWP^{W330R} did not bind to any histone modification represented on the array (Fig. 2e and Supplementary Fig. 1b).

The second mutation, p.D333N, is located at the aspartate residue that forms part of the cage surrounding H3K36me2/3 (Fig. 2b). As substitution of this residue is known to abrogate H3K36me2/3 binding¹⁵, we conclude that both the W330R and D333N substitutions are likely to impair DNMT3A's binding of methylated H3K36.

As the N-terminal and ADD-domains of DNMT3A also mediate chromatin interactions^{20,21}, this suggested that DNMT3A^{W330R} and DNMT3A^{D333N} proteins would have altered chromatin-binding specificity, which in turn could modify the pattern of DNA methylation in patient cells.

Increased DNA Methylation occurs at key developmental genes in patient cells

We therefore assessed the genome-wide distribution of DNA methylation in patient-derived fibroblasts using Illumina Infinium MethylationEPIC beadchips. Unsupervised hierarchical clustering established that dermal primary fibroblasts from *DNMT3A*^{W330R/+} microcephalic dwarfism patients had similar DNA methylation profiles, significantly distinct from those of healthy subjects (Fig. 3a, $p < 0.001$ for each group). 1878 differentially methylated regions (DMRs) were common to both patients (Fig. 3b and Supplementary Fig. 2). Consistent with altered genomic targeting of *DNMT3A*^{W330R}, the majority of DMRs were hypermethylated relative to controls ($n=1140$, Fig. 3b,c and Supplementary Table 2). Notably, the same regions of increased DNA methylation were also present in *DNMT3A*^{W330R/+} patient peripheral blood leukocytes (PBLs) indicating this to be a reproducible signature and not a consequence of *in vitro* culture²² (Fig. 3b,c). Furthermore, the same hypermethylated DMRs were also evident in patient P3's PBLs (Supplementary Fig. 3). In contrast, DMRs hypomethylated in fibroblasts were not observed in patient PBLs ($n=738$; Supplementary Fig. 2a,b, Supplementary Fig. 3b,c and Supplementary Table 3). *DNMT3A*^{W330R} hypermethylated DMRs were not evident in *DNMT3A* overgrowth patient PBLs, (Fig. 3b,c), and were also absent from pericentrin (*PCNT*) null patient fibroblasts indicating they were not a general consequence of microcephalic dwarfism (Supplementary Fig. 2c).

Gene ontology analysis for the genes located closest to the hypermethylated DMRs demonstrated a striking association with transcription factors and developmental processes (Fig. 3d and Supplementary Table 4). Notably multiple Hox, lineage-specific transcription factors and morphogen genes were evident in the DMR gene

list (Fig. 3e). Visual inspection of the DMRs established these regions to contain CpG islands (CGIs) and encompass genomic regions surrounding these developmental genes (Fig. 3f).

Hypermethylation of Polycomb-marked DNA methylation valleys in patient cells

To understand the genomic context of the hypermethylated DMRs, we investigated their chromatin state by intersecting the DMRs with existing ChromHMM annotations for normal human lung fibroblasts (NHLF)²³. The DMRs were significantly enriched for 'Poised-Promoter' and 'Polycomb-Repressed' ChromHMM categories (Fig. 4a), both of which are associated with Polycomb repressive complexes (PRCs). To directly address if these hypermethylated DMRs were Polycomb-marked regions in dermal primary fibroblasts, we next performed ChIP-seq for H3K27me3, the epigenetic signature of the Polycomb repressive complex 2 (PRC2)^{24,25}. Significant enrichment for control fibroblast H3K27me3 peaks was seen at DMR sites ($P < 2.2 \times 10^{-16}$, Fig. 4b-d) confirming them to be normally marked by H3K27me3.

Notably the regions of increased DNA methylation in patient cells were not confined to CGIs and often extended over tens of kilobases of genomic sequence (Fig. 3f). Their extent and location were reminiscent of ordinarily hypomethylated domains, that have been termed 'DNA methylation valleys' (DMVs)^{26,27}, 'DNA methylated canyons'²⁸ or 'broad non-methylated islands'²⁹. These have been demonstrated to be evolutionary conserved regions, often associated with Polycomb-regulated developmental genes. Subsequent analysis confirmed a significant overlap between

genes within reported DMVs²⁶ and genes associated with *DNMT3A*^{W330R/+}

hypermethylated DMRs ($P = 8.3 \times 10^{-170}$, Fig 4e).

Comparison of H3K27me3-marked DMVs in control fibroblasts with those lacking H3K27me3, established that the polycomb-associated DMVs were specifically hypermethylated in patients ($P = 9.6 \times 10^{-83}$, Fig. 4f-h). Subsequent H3K4me3 ChIP-seq showed that hypermethylated DMVs also contained H3K4me3 peaks (Fig. 4f), consistent with ChromHMM 'poised-promoter' predictions (Fig. 4a). DMVs without Polycomb marks exhibited higher levels of H3K4me3 (Fig. 4 g,i), consistent with transcriptionally active loci.

In *DNMT3A*^{W330R/+} patient fibroblasts, H3K27me3 levels were reduced at hypermethylated DMRs and H3K27me3 marked DMVs (Fig. 4f,g, Supplementary Fig. 4a-f). However, levels of the H3K27me3 methyltransferase EZH2 were normal in patient fibroblasts, and total cellular levels of H3K27me3-marked histones were unchanged when assessed by mass-spectroscopy (Supplementary Fig. 4g-i). Therefore, reduction in H3K27me3 was likely the result of DNMT3A-mediated DNA methylation inhibiting PRC2 binding/activity^{30,31}. H3K4me3 levels were also reduced at hypermethylated DMRs and H3K27me3 marked DMVs (Supplementary Fig. 5a-e), significantly more than at other H3K4me3 peaks in the genome, consistent also with this reduction being a secondary consequence of DNA hypermethylation.

We therefore concluded that the W330R mutation is associated with hypermethylation of Polycomb-marked DMVs in patient cells, impacting on bivalent histone marks and modifying the chromatin state at key developmental regulators.

H3K36me3 and H3K27me3 histone modifications are usually mutually exclusive^{32,33}, and strongly anti-correlated genome-wide³⁴. To confirm this was also the case for DMRs and DMVs we performed H3K36me3 ChIP Rx-seq, and indeed few H3K36me3 ChIP-seq reads were present in DMVs in control and patient cells, with no enrichment over ChIP input seen (Supplementary Fig. 6a,b). Furthermore, hypermethylated DMRs in both control and patient fibroblasts were substantially depleted for H3K36me3 ChIP-seq peaks, when compared to all Infinium array probe sites (Supplementary Fig. 6c).

Hypermethylation at Polycomb marked loci occurs upon differentiation of *DNMT3A*^{W326R} pluripotent stem cells

As large scale *de novo* DNA methylation occurs during early embryogenesis prior to implantation³⁵, we reasoned that the increased methylation detected in patient fibroblasts and leukocytes was likely to have developmental origins. We addressed this possibility using the previously generated *Dnmt3a*^{W326R} mES cell lines, containing the W330R-orthologous murine mutation (Fig. 2a). However, bisulfite sequencing of the promoter CpG islands of *Hoxc13*, *Sox1* and *Foxa1* (loci we had established to have increased methylation in patient cells), demonstrated similar low levels of DNA methylation in wild-type, *DNMT3A*^{W326R/+} and *DNMT3A*^{W326R/W326R} ES cells (Fig. 5a and Supplementary Fig. 7a,b). Nevertheless, upon differentiation to embryoid bodies (EBs), DNA hypermethylation became evident in *DNMT3A*^{W326R/+} and *DNMT3A*^{W326R/W326R} cells relative to controls (Fig. 5b). To exclude skewing of lineage fate in EBs as a confounding explanation for altered methylation, directed differentiation of mESCs to neural progenitor cells (NPCs)³⁶ was also performed.

This also demonstrated increased methylation in *DNMT3A*^{W326R} cells (Fig. 5c). Furthermore, Reduced Representation Bisulfite Sequencing (RRBS)³⁷ established that such methylation occurred at many Polycomb-marked loci in neurally-differentiated cells (Fig. 5d,e). 342 hypermethylated DMRs were detected in *DNMT3A*^{W326R/W326R} cells relative to wild-type controls (Supplementary Table 5). These regions were significantly enriched for H3K27me3 ChIP-seq peaks derived from a wildtype neural-progenitor differentiation dataset³⁸ ($P < 2.2 \times 10^{-16}$, Fig. 5e). As well, 105 of 207 DMR-associated genes overlapped orthologous gene loci for hypermethylated patient fibroblast DMRs ($P = 1.7 \times 10^{-71}$ Fisher's exact test, Fig. 5f). Therefore, we conclude that the W326R substitution causes methylation at Polycomb-marked developmental genes from early stages of cell fate specification and differentiation *in vitro*.

Neurogenic gene expression bias in *Dnmt3a*^{W326R} NPCs

To understand the transcriptional consequences of DMR hypermethylation, we next performed RNA-seq on *Dnmt3a*^{W326R/W326R} NPCs and *DNMT3A*^{W330R/+} fibroblasts. We found a significant downregulation of transcription of genes associated with hypermethylated DMRs, whereas transcript levels at hypomethylated DMRs were unchanged (Fig. 5g and Supplementary Fig. 8a-c). We reasoned that many of the DMR/DMV-associated genes are transcription factors, that would consequently perturb developmental transcriptional networks. Prior work has demonstrated differentiation to be impaired in *Dnmt3a*-deficient NPCs and hematopoietic stem cells (HSCs) with enhanced expression of multipotency/stem cell genes and decreases in differentiation/neurogenic gene transcripts^{31,39,40}. As W326R is a 'gain of function' mutation, we postulated that a reciprocal transcriptional phenotype would be evident

in *Dnmt3a*^{W326R/W326R} NPCs. Accordingly, we examined two gene sets, representing genes that are respectively up and down-regulated during differentiation of mESCs to terminally-differentiated neurons³⁸ (Fig. 5h). In line with our expectation, *Dnmt3a*^{W326R/W326R} NPCs demonstrated a transcriptional bias towards expression of neurogenic genes at the expense of genes normally expressed in the pluripotent state. This suggests that hypermethylation of DMV/DMRs could lead to a skewing of stem/progenitor cells towards differentiation away from self-renewal.

***Dnmt3a*^{W326R/+} mice have reduced brain size and body weight**

Finally, we generated a *Dnmt3a*^{W326R/+} mouse using CRISPR/Cas9-mediated homology directed repair (Supplementary Fig. 9a,b) to provide an *in vivo* model. Recapitulating the patient growth restriction phenotype, *Dnmt3a*^{W326R/+} mice were viable, healthy and morphologically unremarkable, but were proportionately small with significantly reduced body and brain weight (Fig. 6a-c, Supplementary Fig 9c,d). Furthermore, bisulfite sequencing of cerebral cortex and liver provided *in vivo* confirmation of hypermethylation at polycomb-regulated regions, with substantial methylation observed at the *Hoxc13* and *Sox1* loci in *Dnmt3a*^{W326R/+} mice (Fig. 6d, Supplementary Fig. 9e). Furthermore, RRBS analysis confirmed that genome-wide, NPC hypermethylated DMRs were hypermethylated in the *Dnmt3a*^{W326R/+} mouse cortex (Supplementary Fig. 9f-h).

Discussion

Here we report widespread DNA hypermethylation at Polycomb-regulated regions resulting from a gain of function mutation in *DNMT3A*. As such genomic regions contain key developmental genes, classical patterning defects might be expected,

but, surprisingly, the DNMT3A^{W330R} mutation instead causes an extreme growth disorder.

Unexpectedly our findings suggest that the DNMT3A PWWP domain limits DNA methylation at Polycomb-regulated regions. DNMT3A has been previously shown to counter H3K27 tri-methylation *in vivo*, with wild-type (but not catalytically dead) DNMT3A opposing PRC2 binding in neural stem cells³¹. In patient cells, it is therefore likely that altered binding specificity of DNMT3A^{W330R} leads to it methylating polycomb-associated DMRs and DMVs, with a secondary reduction occurring in H3K27me3 due to impaired binding of PRC2 to methylated DNA^{30,31}. Biochemically, binding to H3K36me2/3 is abrogated in the PWWP^{W330R} mutant. How then could this impaired interaction with H3K36me2/3 connect with DNA methylation of H3K27me3 regions? We favour a model where widespread distribution of H3K36me2/3 leads to wild-type DNMT3A being targeted to many genomic sites and limiting its availability to non-preferred sites such as polycomb-associated regions (Fig 6e). Consistent with this model, we see low levels of H3K36me3 at DMRs and DMVs, explained by H3K36me2/3 rarely co-existing with H3K27me3 on histones^{32,33}. As well, genome-wide, H3K36me3 is strongly anticorrelated with H3K27me3, and low levels of H3K36me2 correlated with increased H3K27me3³⁴. Furthermore, H3K36me2 is actively removed by KDM2A from unmethylated CpG regions⁴¹ and Nsd1-mediated H3K36me2 methylation has recently been shown to restrict deposition of H3K27me3³⁴.

In our model we propose that disruption of PWWP-H3K36me2/3 interactions in patient cells would increase availability of DNMT3A^{W330R} to interact with DNA in

polycomb regions (Fig 6e), increasing the possibility of DNA methylation, consequently impairing PRC2 binding and polycomb-domain integrity. Alternative explanations are also possible. For instance, the PWWP^{WT}-H3K36me2/3 interaction may normally be required for enzymatic activity, whereas DNMT3A^{W330R} may be permissive for DNA methylation without the interaction; or the PWWP domain may mediate non-histone interactions critical to restrict it from Polycomb-marked loci. Further studies, including assessment of DNMT3A^{W330R} localization by ChIP-seq to determine genomic distribution, will be important in distinguishing between these possibilities. Nonetheless, our findings establish the DNMT3A PWWP domain as a factor countering methylation of key developmental loci, one that may act alongside Tet enzymes^{42,43} and FBXL10⁴⁴ to ensure their hypomethylation.

Previously identified microcephalic dwarfism genes impair cell proliferation to reduce cell number and organism size¹, so how might this mutation in *DNMT3A* act? Both DNA methyltransferases and Polycomb can impart heritable transcriptionally repressive epigenetic marks. However, while DNA promoter methylation is considered to stably silence genes⁴⁵, Polycomb repression is potentially reversible, maintaining plasticity of gene expression and enabling robust switching to gene activation in response to developmental cues^{46,47}. Dnmt3a loss in hematopoietic stem cells leads to expanded stem cell numbers at a cost to differentiated progeny³⁹. Likewise, Dnmt3a null neural stem cells have markedly reduced neurogenic potential³¹. Conversely, loss of the PRC2 H3K27me3 methyltransferase, Ezh2, from cortical progenitors impairs self-renewal promoting premature neuronal differentiation⁴⁸, and here we observe a transcriptional bias away from pluripotency towards differentiation in Dnmt3a^{W326R/W32R} NPCs (Fig 5.). Hence, gain of function

DNMT3A mutations might increase cellular differentiation leading to premature depletion of stem/progenitor cell pools and reduce final cell numbers in tissues and consequently organism size (Supplementary Fig. 8d).

Like DNMT3A, haploinsufficiency of H3K36 methyltransferases NSD1 and SETD2, cause macrocephalic overgrowth^{13,49,50}. Mutations in genes encoding EZH2, and EED subunits of Polycomb complexes also cause overgrowth⁵¹⁻⁵³ and PHC1 mutation results in microcephalic dwarfism⁵⁴. While DNA methylation and Polycomb-repression are thought of as mutually antagonistic and exclusive processes at specific loci, our findings linking H3K27, H3K36 and DNA methylation, suggest a yet to be defined common developmental mechanism for these syndromes.

Furthermore, given *NSD1*, *DNMT3A* and *EZH2* are both height QTLs and somatically mutated in cancer^{55,56}, the interplay between Polycomb and DNA methylation has wider relevance both to neoplastic processes and physiological regulation of human size, that warrants further investigation.

Accession Codes:

DNMT3A –NM_175629.2

EGA: WES data: EGAS00001003231; RNAseq/RRBS/ChIPseq EGAS00001003232

GEO: awaiting accession codes

Acknowledgements:

We are grateful to families and clinicians for their involvement and participation. We would like to thank W. Bickmore, R. Meehan, N. Hastie, T. Baubec and I. Adams for helpful discussions. G. Kelsey for discussion of unpublished data. P. Madapura, G.

Taylor, L. Duthie and R. Illingworth for technical advice, E. Freyer, A. Meynert, IGMM FACS and Sequencing Cores, CBS, WTCCB mass-spectroscopy facility and the WTCRF for technical support. A.P.J. is supported by the Medical Research Council UK (MRC, U127580972) and the European Research Council (ERC), through ERC Starter Grant 281847; and now by the European Union's Horizon 2020 research and innovation programme ERC Advanced Grant (grant agreement No: 788093). D.S. is a Cancer Research UK Career Development Fellow (reference C47648/A20837), and work in his laboratory is also supported by a Medical Research Council University grant to the MRC Human Genetics Unit. J.M. is supported by a Medical Research Council Career Development Award (MR/M02122X/1). P.H. was supported by a fellowship within the Postdoc-Program of the German Academic Exchange Service (DAAD). V. Hwa is supported by funding from NIH NICHD R01HD078592. T.A. is supported by Wellcome Trust funding to R.C.A. (200885). J.R. is supported by the Wellcome Trust through a Senior Research Fellowship (103139) and a multi-user equipment grant (108504). The Wellcome Centre for Cell Biology is supported by core funding from the Wellcome Trust (203149).

Author Contributions:

CVL, RCC, DAP, AD performed molecular genetic studies to identify patient mutations. PH designed the cell biology experiments, and performed these with CVL, AF, FT, FK and MAMR. PH, AF and CAM characterized the mouse model. JAM performed structural modelling. TA performed mass spectrometry with support from RCA and JR. VCD, CTF, KG, VH, LI, SPR, GS, and AD ascertained subjects, obtained samples and/or assisted with clinical studies. DS performed computational analyses of DNA methylation, ChIPseq and RNAseq datasets. PH, DS and APJ wrote the

394 manuscript with input from MAMR, and all authors reviewed it. DS and APJ
395 planned and supervised the study.

396

397 **Competing Interests:**

398 The authors declare no competing interests.

399 **References:**

- 400 1. Klingseisen, A. & Jackson, A.P. Mechanisms and pathways of growth failure in
401 primordial dwarfism. *Genes and Development* **25**, 2011-2024 (2011).
- 402 2. Bicknell, L.S. *et al.* Mutations in the pre-replication complex cause Meier-Gorlin
403 syndrome. *Nat Genet* **43**, 356-9 (2011).
- 404 3. Bicknell, L.S. *et al.* Mutations in ORC1, encoding the largest subunit of the origin
405 recognition complex, cause microcephalic primordial dwarfism resembling Meier-
406 Gorlin syndrome. *Nat Genet* **43**, 350-5 (2011).
- 407 4. Guernsey, D.L. *et al.* Mutations in origin recognition complex gene ORC4 cause
408 Meier-Gorlin syndrome. *Nat Genet* **43**, 360-4 (2011).
- 409 5. Burrage, L.C. *et al.* De Novo GMNN Mutations Cause Autosomal-Dominant
410 Primordial Dwarfism Associated with Meier-Gorlin Syndrome. *Am J Hum Genet* **97**,
411 904-13 (2015).
- 412 6. Rauch, A. *et al.* Mutations in the pericentrin (PCNT) gene cause primordial dwarfism.
413 *Science* **319**, 816-9 (2008).
- 414 7. Griffith, E. *et al.* Mutations in pericentrin cause Seckel syndrome with defective ATR-
415 dependent DNA damage signaling. *Nat Genet* **40**, 232-6 (2008).
- 416 8. Martin, C.A. *et al.* Mutations in PLK4, encoding a master regulator of centriole
417 biogenesis, cause microcephaly, growth failure and retinopathy. *Nat Genet* **46**, 1283-
418 92 (2014).
- 419 9. Conlon, I. & Raff, M. Size control in animal development. *Cell* **96**, 235-44 (1999).
- 420 10. Lek, M. *et al.* Analysis of protein-coding genetic variation in 60,706 humans. *Nature*
421 **536**, 285-91 (2016).
- 422 11. Tatton-Brown, K. *et al.* Mutations in the DNA methyltransferase gene DNMT3A cause
423 an overgrowth syndrome with intellectual disability. *Nat Genet* **46**, 385-8 (2014).
- 424 12. Tlemsani, C. *et al.* SETD2 and DNMT3A screen in the Sotos-like syndrome French
425 cohort. *J Med Genet* (2016).
- 426 13. Okamoto, N., Toribe, Y., Shimojima, K. & Yamamoto, T. Tatton-Brown-Rahman
427 syndrome due to 2p23 microdeletion. *Am J Med Genet A* **170A**, 1339-42 (2016).
- 428 14. Ran, F.A. *et al.* Genome engineering using the CRISPR-Cas9 system. *Nat Protoc* **8**,
429 2281-2308 (2013).
- 430 15. Dhayalan, A. *et al.* The Dnmt3a PWWP domain reads histone 3 lysine 36
431 trimethylation and guides DNA methylation. *J Biol Chem* **285**, 26114-20 (2010).
- 432 16. Sankaran, S.M., Wilkinson, A.W., Elias, J.E. & Gozani, O. A PWWP Domain of Histone-
433 Lysine N-Methyltransferase NSD2 Binds to Dimethylated Lys-36 of Histone H3 and
434 Regulates NSD2 Function at Chromatin. *J Biol Chem* **291**, 8465-74 (2016).
- 435 17. Qin, S. & Min, J. Structure and function of the nucleosome-binding PWWP domain.
436 *Trends Biochem Sci* **39**, 536-47 (2014).
- 437 18. Rondelet, G., Dal Maso, T., Willems, L. & Wouters, J. Structural basis for recognition
438 of histone H3K36me3 nucleosome by human de novo DNA methyltransferases 3A
439 and 3B. *J Struct Biol* **194**, 357-67 (2016).
- 440 19. Kungulovski, G. *et al.* Application of histone modification-specific interaction
441 domains as an alternative to antibodies. *Genome Res* **24**, 1842-53 (2014).
- 442 20. Du, J., Johnson, L.M., Jacobsen, S.E. & Patel, D.J. DNA methylation pathways and
443 their crosstalk with histone methylation. *Nat Rev Mol Cell Biol* **16**, 519-32 (2015).

- 444 21. Manzo, M. *et al.* Isoform-specific localization of DNMT3A regulates DNA methylation
445 fidelity at bivalent CpG islands. *EMBO J* **36**, 3421-3434 (2017).
- 446 22. Meissner, A. *et al.* Genome-scale DNA methylation maps of pluripotent and
447 differentiated cells. *Nature* **454**, 766-70 (2008).
- 448 23. Ernst, J. *et al.* Mapping and analysis of chromatin state dynamics in nine human cell
449 types. *Nature* **473**, 43-9 (2011).
- 450 24. Cao, R. *et al.* Role of histone H3 lysine 27 methylation in Polycomb-group silencing.
451 *Science* **298**, 1039-43 (2002).
- 452 25. Kuzmichev, A., Jenuwein, T., Tempst, P. & Reinberg, D. Different EZH2-containing
453 complexes target methylation of histone H1 or nucleosomal histone H3. *Mol Cell* **14**,
454 183-93 (2004).
- 455 26. Xie, W. *et al.* Epigenomic analysis of multilineage differentiation of human
456 embryonic stem cells. *Cell* **153**, 1134-48 (2013).
- 457 27. Li, Y. *et al.* Genome-wide analyses reveal a role of Polycomb in promoting
458 hypomethylation of DNA methylation valleys. *Genome Biol* **19**, 18 (2018).
- 459 28. Jeong, M. *et al.* Large conserved domains of low DNA methylation maintained by
460 Dnmt3a. *Nat Genet* **46**, 17-23 (2014).
- 461 29. Long, H.K. *et al.* Epigenetic conservation at gene regulatory elements revealed by
462 non-methylated DNA profiling in seven vertebrates. *Elife* **2**, e00348 (2013).
- 463 30. Bartke, T. *et al.* Nucleosome-interacting proteins regulated by DNA and histone
464 methylation. *Cell* **143**, 470-84 (2010).
- 465 31. Wu, H. *et al.* Dnmt3a-dependent nonpromoter DNA methylation facilitates
466 transcription of neurogenic genes. *Science* **329**, 444-8 (2010).
- 467 32. Sidoli, S. *et al.* Middle-down hybrid chromatography/tandem mass spectrometry
468 workflow for characterization of combinatorial post-translational modifications in
469 histones. *Proteomics* **14**, 2200-11 (2014).
- 470 33. Yuan, W. *et al.* H3K36 methylation antagonizes PRC2-mediated H3K27 methylation. *J*
471 *Biol Chem* **286**, 7983-9 (2011).
- 472 34. Streubel, G. *et al.* The H3K36me2 Methyltransferase Nsd1 Demarcates PRC2-
473 Mediated H3K27me2 and H3K27me3 Domains in Embryonic Stem Cells. *Mol Cell* **70**,
474 371-379 e5 (2018).
- 475 35. Smallwood, S.A. & Kelsey, G. De novo DNA methylation: a germ cell perspective.
476 *Trends Genet* **28**, 33-42 (2012).
- 477 36. Pollard, S.M., Benchoua, A. & Lowell, S. Neural stem cells, neurons, and glia.
478 *Methods Enzymol* **418**, 151-69 (2006).
- 479 37. Meissner, A. *et al.* Reduced representation bisulfite sequencing for comparative
480 high-resolution DNA methylation analysis. *Nucleic Acids Res* **33**, 5868-77 (2005).
- 481 38. Tippmann, S.C. *et al.* Chromatin measurements reveal contributions of synthesis and
482 decay to steady-state mRNA levels. *Mol Syst Biol* **8**, 593 (2012).
- 483 39. Challen, G.A. *et al.* Dnmt3a is essential for hematopoietic stem cell differentiation.
484 *Nat Genet* **44**, 23-31 (2011).
- 485 40. Jeong, M. *et al.* Loss of Dnmt3a Immortalizes Hematopoietic Stem Cells In Vivo. *Cell*
486 *Rep* **23**, 1-10 (2018).
- 487 41. Blackledge, N.P. *et al.* CpG Islands Recruit a Histone H3 Lysine 36 Demethylase.
488 *Molecular Cell* **38**, 179-190 (2010).
- 489 42. Wiehle, L. *et al.* Tet1 and Tet2 Protect DNA Methylation Canyons against
490 Hypermethylation. *Mol Cell Biol* **36**, 452-61 (2015).

491 43. Gu, T. *et al.* DNMT3A and TET1 cooperate to regulate promoter epigenetic
492 landscapes in mouse embryonic stem cells. *Genome Biol* **19**, 88 (2018).
493 44. Boulard, M., Edwards, J.R. & Bestor, T.H. FBXL10 protects Polycomb-bound genes
494 from hypermethylation. *Nat Genet* **47**, 479-85 (2015).
495 45. Goll, M.G. & Bestor, T.H. Eukaryotic cytosine methyltransferases. *Annu Rev Biochem*
496 **74**, 481-514 (2005).
497 46. Voigt, P., Tee, W.W. & Reinberg, D. A double take on bivalent promoters. *Genes Dev*
498 **27**, 1318-38 (2013).
499 47. Klose, R.J., Cooper, S., Farcas, A.M., Blackledge, N.P. & Brockdorff, N. Chromatin
500 sampling--an emerging perspective on targeting polycomb repressor proteins. *PLoS*
501 *Genet* **9**, e1003717 (2013).
502 48. Pereira, J.D. *et al.* Ezh2, the histone methyltransferase of PRC2, regulates the
503 balance between self-renewal and differentiation in the cerebral cortex. *Proc Natl*
504 *Acad Sci U S A* **107**, 15957-62 (2010).
505 49. Kurotaki, N. *et al.* Haploinsufficiency of NSD1 causes Sotos syndrome. *Nat Genet* **30**,
506 365-6 (2002).
507 50. Luscan, A. *et al.* Mutations in SETD2 cause a novel overgrowth condition. *J Med*
508 *Genet* **51**, 512-7 (2014).
509 51. Tatton-Brown, K. *et al.* Germline mutations in the oncogene EZH2 cause Weaver
510 syndrome and increased human height. *Oncotarget* **2**, 1127-33 (2011).
511 52. Gibson, W.T. *et al.* Mutations in EZH2 cause Weaver syndrome. *Am J Hum Genet* **90**,
512 110-8 (2012).
513 53. Cohen, A.S. *et al.* A novel mutation in EED associated with overgrowth. *J Hum Genet*
514 **60**, 339-42 (2015).
515 54. Awad, S. *et al.* Mutation in PHC1 implicates chromatin remodeling in primary
516 microcephaly pathogenesis. *Hum Mol Genet* **22**, 2200-13 (2013).
517 55. Tatton-Brown, K. *et al.* Mutations in Epigenetic Regulation Genes Are a Major Cause
518 of Overgrowth with Intellectual Disability. *Am J Hum Genet* **100**, 725-736 (2017).
519 56. Wood, A.R. *et al.* Defining the role of common variation in the genomic and
520 biological architecture of adult human height. *Nat Genet* **46**, 1173-86 (2014).
521 57. Ernst, J. & Kellis, M. Chromatin-state discovery and genome annotation with
522 ChromHMM. *Nat Protoc* **12**, 2478-2492 (2017).
523

Fig. 1| De novo mutations in DNMT3A cause microcephalic dwarfism.

a, Schematic of DNMT3A protein and domains. Position of microcephalic dwarfism (MD) mutations (red) and Tatton-Brown-Rahman syndrome (TBRS) overgrowth (grey) mutations (Tatton-Brown et al. 2014) (MTase, DNA methyltransferase domain)

b, The heterozygous *de novo* c.988T>C mutation results in substitution of a Tryptophan residue (patient 1 and 2). The heterozygous *de novo* c.997G>A mutation results in substitution of an Aspartic acid residue (patient 3). Both residues are conserved in vertebrates **c**, and replaced with a physiochemically dissimilar residue: Arginine (p.W330R) and Asparagine (p.D333N) respectively. Sequence alignments, Clustal Omega. **d**, The W330R and D333N mutations cause extreme growth failure and microcephaly (red diamonds, n=3 independent patients), in direct contrast to DNMT3A overgrowth patients (grey circles, n=13 and n=12 patients, respectively for height and OFC). Height and head circumference (OFC) plotted as z-scores (s.d. for population mean adjusted for age and sex). Dashed lines at -2 and +2 s.d indicate 95% confidence interval for general population. Horizontal bars, mean values for respective patient groups. TBRS morphometric data reproduced from Tatton-Brown et al. 2014¹¹.

Fig. 2| The W330R mutation impairs binding of di/tri-methylated H3K36.

a, Murine Dnmt3a^{W326R} protein, containing the orthologous substitution to W330R, is stably expressed, in contrast to corresponding overgrowth PWWP mutations (W293del, I306N). Immunoblotting of cell lysates from CRISPR/Cas9 genome-edited mouse embryonic stem cells (mESC). Multiple independent cell lines, with genotypes as indicated. Representative of n=3 (WT, W326R lines) and n=2 (W293del, I306N) independent experiments. Immunoblots are cropped. **b**, Structural modelling of the PWWP domain predicts the W330R mutation to disrupt interaction with H3K36me3. The highlighted amino acids (blue) form a cage that binds trimethylated lysine 36 (purple). The amino acids altered in MD patients (tryptophan at codon 330 and aspartate at codon 333) are labelled in red. Backbones of PWWP and histone H3 N-terminal tail depicted in grey and pink respectively. **c,d**, Recombinant PWWP^{WT} but not PWWP^{W330R} protein binds H3K36me3 peptide. **(c)** Schematic of streptavidin pull-down of biotinylated histone peptides. **(d)** Coomassie stained gel of eluted protein from histone peptide pull-downs (cropped). Input, 9% of total protein. Histone peptide H3 (aa 21-44). H3K36me0 corresponding unmodified peptide. Representative of n=3 expts. **e**, PWWP^{W330R} does not bind H3K36me2, H3K36me3 or other histone-tail modifications. MODified™ Histone Peptide Array representing 384 distinct or combinatorial histone modifications probed with recombinant PWWP proteins as indicated. Below, magnified insets of row L7-11 (histone 3 aa26-45) and K1-3 (histone 3 aa16-35) demonstrates that PWWP^{WT} binds to H3K36me2 (L9) and H3K36me3 (L10), but PWWP^{W330R} does not. Representative of n = 2 independent expts; see also Supplementary Fig. 1b.

Fig. 3| DNA methylation is increased at key developmental gene loci in patient cells.

a, DNA methylation in *DNMT3A*^{W330R/+} patient fibroblasts significantly differs from controls. Unsupervised Ward clustering based on Pearson correlations of all probes from Illumina EPIC arrays for n=2 independent patients and 2 independent controls. *Pvclust*, approximately-unbiased *p*-values using 1000 bootstraps. **b,c**, A methylation signature is evident in *DNMT3A*^{W330R} patient cells across tissues, comprising 1140 sites of increased methylation. **(b)** Heat map of differentially methylated regions (DMRs) hypermethylated in patient fibroblasts and peripheral blood leukocytes (PBLs). P1, P2, patients (*DNMT3A*^{W330R/+}); C1-C4 healthy controls; O1, O2, TBRS overgrowth patients. **(c)** Quantification of DNA methylation for DMRs (n=1140 DMRs) depicted in panel **(b)**. Box, 25th-75th percentile; whiskers, full data range; centre line, median; Δ%*mCpG*, percent change of methylation relative to mean of control. *p* value, two-sided, paired Wilcoxon rank sum tests for mean of control probes vs mean patient probes. **d**, Gene ontology analysis of genes associated with hypermethylated DMRs. Top ten significant hits shown. Color indicates Benjamini-Hochberg adjusted FDR significance level, genes associated with DMR probes (n=907 genes) versus genes associated with all probes on the array (n=18159), two-sided Fisher's exact test. **e**, Exemplars of DNA binding factors and morphogens associated with DMRs. **f**, Representative genome browser views of hypermethylated DMRs demonstrating increased DNA methylation at key developmental genes in microcephalic dwarfism patient samples. All tracks scaled 0-100% *mCpG*, DNA methylation. CGI, CpG islands.

Fig. 4| DNA methylation is increased at polycomb-marked DNA methylation valleys.

a, Hypermethylated DMRs in *DNMT3A*^{W330R} patient cells are significantly enriched at poised promoters and polycomb-repressed regions. Plotted, enrichment of chromatin state categories as identified in normal human lung fibroblasts (NHLF) by ChromHMM in patient hypermethylated DMRs. P-values for each enriched category, two-sided Fisher's exact test hyper-DMR probes (n=10871 probes) vs all probes (n=403348). (ChromHMM: software annotating Chromatin state by a Hidden Markov Model)⁵⁷. **b-d**, H3K27me3 sites in control dermal fibroblasts correlate with hypermethylated DMRs in patient cells. **(b)** Heat map of normalised H3K27me3 ChIP-seq reads in control fibroblasts (mean of C1, C2) centred on DMRs, ranked by DMR mean H3K27me3 levels. Scale indicates normalised read counts. Window size, 250 bp. **(c,d)** Quantification of H3K27me3 enrichment at hypermethylated DMRs. **(c)** Percentage of Infinium array probes overlapping H3K27me3 peaks in control fibroblasts (red, mean of C1 and C2). All, all probes on the array (n=403348 probes). Hyper-DMRs, probes within hypermethylated DMRs (n=10871). p-value, two-sided Fisher's exact test. **(d)** Venn diagram displaying overlap of hypermethylated DMRs (n=1140) with H3K27me3 peaks (n=3815) in controls. p value, two-sided Fisher's exact test. **(e)** Genes associated with hypermethylated DMRs (n=907 genes), significantly overlap genes associated with DMVs (n=1,358). Two-sided Fisher's exact test, genes associated with hyper-DMRs vs all genes represented on array. **(f)** Increased methylation is distributed across H3K27me3 regions, but excluded from H3K4me3 peaks. Representative IGV genome browser views. For all tracks: DNA methylation (magenta, scale 0-100%), H3K27me3 (green, scale 0-4 scaled read counts per 10⁷ reads), H3K4me3 (yellow, scale 0-8 scaled read counts per 10⁷ reads) in control (C1, C2) and patient (P1, P2) dermal fibroblasts. DNA methylation data for *SOX1* and *FOXA1* (Fig. 3f) are shown again for comparison with H3K27me3 and H3K4me3. **g**, Polycomb-marked DNA methylation valleys (DMVs) are hypermethylated in *DNMT3A*^{W330R/+} patients. Shown, heat maps of n=1,152 DMVs²⁶ of normalised H3K27me3/K4me3 read counts for control (C1,C2 mean) and patient (P1,P2 mean) fibroblasts, centred on DMVs and ranked by mean H3K27me3 levels in controls. Δ%*mCpG*, percent change of DMV methylation relative to mean of controls. Window size, 500bp. **h, i**, Quantification of data shown in panel **g**. **(h)** Polycomb-marked DMVs exhibit increased methylation in patient cells, while non-

polycomb associated regions do not. Y-axis indicates mean difference between patients and controls: 0, no change; >0 increased in patients; <0 decreased in patients. (i) Polycomb-marked DMVs with increased methylation in patient cells, exhibit lower levels of H3K4me3 in controls (C1, C2 mean). Box, 25th-75th percentile; (h) whiskers, full data range; (i) whiskers, 1.5x interquartile range; centre line, median. Polycomb marked DMV definition, see methods. (p-values in h,i, two-sided Wilcoxon rank sum tests, polycomb positive (+) (n=524) versus negative (-) (n=628) DMVs).

Fig. 5| Hypermethylation of polycomb-marked regions is observed on differentiation of Dnmt3a^{W326R} pluripotent stem cells.

a-e, DNA methylation at DMRs occurs during cellular differentiation to embryoid bodies (EBs) and neural progenitor cells (NPCs) in CRISPR/Cas9-edited Dnmt3a^{W326R} mESCs. Bisulfite sequencing of the *Hoxc13* locus of (a) LIF/serum maintained mESCs, (b) after 9 days differentiation to EBs and (c) after 9 days neural induction to NPCs. For EBs and NPC differentiation, representative of n=2 independent experiments each. Blocks, independent cell lines; open and closed circles, unmethylated and methylated CpGs, respectively; dots, undetermined methylation status; columns CpG sites; rows individual sequences. Total percentage methylation calculated per sample. (d) Genome browser view of RRBS DNA methylation profiles after 9 days neural differentiation. Tracks, independent wild type (dark grey), and Dnmt3a^{W326R} (blue) cell lines. Neural precursor cell H3K27me3 data (magenta) from published ChIP-seq dataset³⁸. DNA methylation (scale 0-80%, all tracks). (e) Hypermethylated DMRs are enriched for H3K27me3 peaks in wildtype NPCs. Percentage of CpGs observed in RRBS overlapping with H3K27me3 peaks. H3K27me3 data from wild type NPC ChIP-seq dataset³⁸. All, all CpGs observed (n=1178718 CpGs). Hyper-DMRs, CpGs within hypermethylated DMRs (3117). P-value, two-sided Fisher's exact test. f, Hypermethylated gene loci in Dnmt3a^{W326R} NPCs substantially overlap those in patient cells. Venn diagram of orthologous genes (human n=781; mouse n=207) associated with respective DMRs. P-value, two-sided Fisher's exact test. (g) Reduced expression for genes associated with hyper-DMRs is evident during NPC differentiation. RNA-seq data for NPC differentiation experiment from panel d. (n=3 wild-type clones, n=3 Dnmt3a^{W326R/W326R} clones). log2 CPM ratios of Dnmt3a^{W326R/W326R} versus wildtype at 9 day NPC differentiation plotted. Box, 25th-75th percentile; whiskers, 1.5x interquartile range from box; centre line, median. Two-sided Wilcoxon rank sum test, All genes with coverage in RRBS (n=12620 genes) vs genes associated with hypo-DMRs (n=169) or hyper-DMRs (n=161). **h-i**, Neurogenic gene transcription bias in Dnmt3a^{W326R/W326R} NPCs. (h) log2 CPM ratios of genes for Dnmt3a^{W326R/W326R} versus wild-type 9 day-differentiated NPCs. All, all genes n=13,022; and gene sets, upregulated (n=3,864 genes), unchanged (n=3,516) and downregulated genes (n=3,281) during differentiation from mESCs to neurons. Box, 25th-75th percentile; whiskers, 1.5x interquartile range from box; centre line, median. Two-sided Wilcoxon

668 rank sum test, log₂ W326R/WT for All vs up or downregulated gene sets. (i)
669 Schematic: Gene sets defined on basis of published dataset of mESC differentiation
670 to terminally differentiated neurons³⁸. Downregulated and upregulated gene sets
671 defined as those genes with reduced and increased transcripts respectively in
672 neurons relative to ES cells. The downregulated set therefore contains pluripotency-
673 related genes (light blue) and the upregulated set, neuronal differentiation genes
674 (light red).
675

Fig. 6| Dnmt3a^{W326R/+} mice have reduced brain size and body weight, alongside hypermethylation of developmental genes.

a, 10-week old *Dnmt3a*^{W326R/+} mouse next to wild-type littermate. **(b)** Body weight for 6 week-old *Dnmt3a*^{W326R/+} mice compared to wild type littermates. Males, n=14 wildtype and n=18 *Dnmt3a*^{W326R/+} animals. Females, n= 16 wildtype and n=23 *Dnmt3a*^{W326R/+} animals. **(c)** Brain weight of female *Dnmt3a*^{W326R/+} mice compared to wild type litter mates at 5 months of age. n=7 wildtype and 9 *Dnmt3a*^{W326R/+} animals. **(d)** Locus-specific (*Hoxc13*) bisulfite sequencing for cortex and liver samples from *Dnmt3a*^{W326R/+} and wild-type littermates (n=3/group; female, age 8 weeks). **e**, Proposed model linking disruption of the H3K36me2/3<--> PWWP interaction with DMV DNA methylation. WT-DNMT3A is normally targeted to H3K36me2 and H3K36me3, marks present widely in the genome^{32,58}, but rarely coexist with H3K27me3^{32,33}. This limits availability of free-DNMT3A to bind at other locations. When the PWWP-H3K36me2/3 interaction is disrupted, sufficient free DNMT3A is available to methylate genomic DNA at DMVs. Enzymatic activity of DNMT3A and DNA methylation impair PRC2 chromatin binding^{30,31}, leading to secondary loss of H3K27me3. Notably, the long isoform of DNMT3A (DNMT3A1) localises to the edge of Polycomb domains^{21,43}. When mutated it is therefore well placed to methylate these regions. DNMT3A1 is also the major isoform expressed after ESC differentiation²¹, potentially explaining timing of hypermethylation. Filled circles methylated CpG, open circles unmethylated CpG. Diamonds, H3K36me2/3 modified histones.

Materials and Methods

Research subjects

Genomic DNA from affected children and family members was extracted using standard protocols. Informed, written consent was obtained from all participating families. The study was approved by the Scottish Multicentre Research Ethics Committee (04:MRE00/19) and the Institutional Review Board of Cincinnati Children's Hospital Medical Center (Protocol#2014-5919). All relevant ethical regulations were followed. Genotypes of TBRS patients were as follows: O1: DNMT3A – heterozygous c.1936G>C p.Gly464Arg; O2: DNMT3A – heterozygous c.2086del p.Gln696ArgFsTer9.

Exome sequencing

Exome sequencing of patients 1 and 3 was performed by Edinburgh Genomics and Cincinnati Children's Hospital Sequencing Core Facility respectively as described previously^{59,60}. Patient 2 was sequenced by Illumina MiSeq using a custom targeted capture (SureSelect, Agilent Technologies) targeting DNMT3A and other primordial dwarfism/microcephaly genes. Confirmatory Sanger sequencing was performed on all affected individuals and their parents. Primers listed in Supplementary Table 6. Further details see Supplementary Note.

Cell culture

Primary fibroblast cell lines were maintained at 3% O₂ in Dulbecco's modified Eagle's medium (DMEM; Life Technologies) supplemented with 10% FBS and 5% penicillin-streptomycin antibiotics or in AmnioMAX-C100 (Life Technologies). HeLa

cells, a kind gift from G. Stewart (Birmingham) originally obtained from ATCC, were maintained in Dulbecco's modified Eagle's medium (DMEM; Life Technologies) supplemented with 10% FBS and 5% penicillin-streptomycin antibiotics. E14 Tg2a IV mESCs were cultured on 0.1% gelatine coated dishes and maintained in Glasgow's Minimum Essential Medium (GMEM; Life Technologies) supplemented with 10% FBS (HyClone), 1 mM Sodium Pyruvate (Sigma); 1x MEM non-essential amino acids (Sigma), 2 mM L-Glutamine, 5% penicillin-streptomycin antibiotics, 0.001% β -mercaptoethanol (Sigma) and leukemia inhibitory factor. Details for differentiation protocols see Supplementary Note.

Generation of CRISPR/Cas9 edited mESCs

Guide RNAs were designed using the optimized CRISPR design webtool (<http://crispr.mit.edu/>) with corresponding oligonucleotides cloned into pSpCas9(BB)-2A-GFP or pSpCas9n(BB)-2A-GFP (kind gift from Feng Zhang, Addgene Plasmids pX458:#48138, pX461:#48140)¹⁴. ssDNA oligonucleotides (ssODN, IDT Ultramers) repair template sequences for homology directed repair listed in Supplementary Table 6. Two independent CRISPR/Cas9 strategies were employed to generate the W326R mutation in the clones used in this study: each using different gRNAs, and either Cas9-nickase (nCas9) or wildtype Cas9 respectively. Vectors containing guide RNA sequences were transfected together with single stranded DNA oligonucleotides using FuGENE HD transfection reagent (Promega). GFP-positive cells were selected by FACS (FACSAriaII, FACSDiva Software Version 6.1.3, Becton-Dickinson) 48 hours after transfection and plated at clonal density. Individual colonies were grown up and validated by Sanger sequencing.

Immunoblot analysis and antibodies

Whole cell extracts for mESCs, human primary Fibroblasts and HeLa cells were obtained by sonication in UTB buffer (8 M urea, 50 mM Tris, pH 7.5, 150 mM β -mercaptoethanol) and analyzed by SDS-PAGE using 4–12% NuPage Bis-Tris Protein gels (Life Technologies) and transferred onto nitrocellulose membrane. Immunoblotting was performed using antibodies to Dnmt3a (Novus Biologicals NB120-13888; 1:500), EZH2 (Cell Signaling #5246S; 1:1000) and Actin (Sigma A2066; 1:5000). Images acquired with ImageQuant LAS 4000. Uncropped images in Supplementary Fig. 11.

RNA interference

EZH2 was targeted with 40nM of an ON-TARGETplus Human siRNA SMARTpool (L-004218-00-0005, Dharmacon) and cells harvested 48 hours after transfection with RNAiMAX (Thermo Fisher).

RT-PCR and RNA-sequencing

RNA was extracted using the RNeasy kit (QIAGEN) according to manufacturer instructions with DNaseI (QIAGEN) treatment. For RT-PCR cDNA was generated using SuperScript III Reverse Transcriptase (Invitrogen) and random primers (Promega). Primers for RT-PCR listed in Supplementary Table 6. For RNA-sequencing, random primed cDNA from poly-A selected RNA was converted into an Illumina sequencing library and single-end 50bp reads generated on an Illumina HiSeq machine (GATC Biotech Konstanz, Germany). RNA-seq data were aligned to the genome using bowtie 2 (v2.3.1). Further data processing details see Supplementary Note. Alignment statistics are provided in

Supplementary Table 7 and summaries of the data are shown in Supplementary Fig. 8a,b.

Structural Modelling

The impact of W330R on the interaction with H3K36me3 was modelled with FoldX⁶¹ using the crystal structure of the DNMT3B PWWP domain bound to H3K36me3 (PDB ID: 5CIU). The change in interaction energy caused by the equivalent W263R mutation in DNMT3B was calculated with the AnalyseComplex function. Since the H3K36me3 binding site is highly conserved between DNMT3A and DNMT3B, including full conservation of all the aromatic residues involved in binding highlighted in Figure 2, this suggests that W330R would also disrupt the interaction.

Generation of recombinant PWWP protein

PWWP domain of DNMT3A was expressed in E.coli and purified using standard methods, documented in the Supplementary Note.

Histone peptide pull downs

20 µg of purified recombinant GST-PWWP fusion protein and 2000 pmol of histone H3 biotinylated peptides (AnaSpec peptides; AS-64440 and AS-64441) were diluted in interaction buffer (50 mM Tris/HCl pH8.0, 100 mM NaCl, 2 mM EDTA, 0.1% Triton X-100 freshly supplemented with 0.5 mM DTT, 0.2 mM PMSF and 1x protease inhibitor cocktail, Roche)¹⁵. Reactions were incubated overnight under rotation at 4°C. MyOne T1 streptavidin beads (Life Technologies) were added to the reactions and rotated for 4h at 4°C, followed by three washes with interaction buffer. 20 µl of sample loading buffer (50 mM Tris pH6.8, 20% Glycerol, 20% SDS, 625 mM β-

mercaptoethanol, bromphenolblue) were added to beads, boiled for 5 min and eluted
proteins separated on 15% SDS-PAGE and visualised with Coomassie Blue R250.

Peptide arrays

Peptide arrays were processed following manufacturer instructions for the MODified
Histone Peptide Arrays (Active Motif). In brief, arrays were blocked and washed with
buffers provided. 10nM or 100nM wildtype or W330R DNMT3A GST-tagged PWWP
protein was diluted in interaction buffer (100 mM KCl, 20 mM Hepes pH7.5, 1 mM
EDTA, 0.1 mM DTT, 10% glycerol)¹⁵ and incubated overnight at 4°C on an orbital
shaker. Protein-peptide interactions were detected with an antibody directed against
the GST-tag (GE Healthcare 27-4577-01; 1:5000) with subsequent ECL-based
detection. c-Myc mouse monoclonal antibody (1:2000, Active-Motif). Images
acquired using ImageQuant LAS 4000.

Infinium® MethylationEPIC BeadChip

Fibroblast genomic DNA extracted using the DNeasy Blood & Tissue Kit (QIAGEN).
DNA was bisulfite converted using the EZ DNA Methylation kit (Zymo Research,
Infinium assay protocol). Infinium® MethylationEPIC BeadChip performed according
to manufacturer instructions by Edinburgh WTCRF. The Bioconductor package *minfi*
(v1.22.1) was used to process raw Infinium *idat* files (ssNoob method)^{62,63}. For
further details, see Supplementary Note. Overall summaries of Infinium methylation
data are shown in Supplementary Figure 10a,b and d.

Chromatin immunoprecipitation and sequencing

Cross-linked chromatin immunoprecipitation was adapted from previous publications^{64,65}, further detailed in the Supplementary Note. For H3K27me3 single-end 50bp reads were generated on an Illumina HiSeq machine (GATC Biotech Konstanz, Germany). For H3K4me3, H3K36me3 ChIP-Rx and H3K27me3 ChIP-Rx single-end 75bp reads were generated on an Illumina NextSeq 550 machine (WTCRF Edinburgh, UK).

ChIP-seq read quality assessment and alignment was performed as for RNA-seq. For ChIP Rx-seq, reads were aligned to a combination of the hg19 and dm6 genomes using the same settings. Multi-mapping reads excluded as for RNA-seq. Additionally, PCR duplicates excluded using SAMBAMBA (v0.5.9)⁶⁶. Sequencing statistics are shown in Supplementary Table 8. For further analysis details see Supplementary Note.

Histone acid extraction and histone PTM detection by mass spectrometry

Histones were acid extracted as previously described³² with minor modifications and LC MS/MS analyses were performed on an Orbitrap Fusion Lumos coupled to Dionex Ultimate3000RSLCnano UHPLC system. For further details see Supplementary Note.

Bisulfite PCR sequencing

Genomic DNA was isolated using the DNeasy Blood & Tissue Kit (QIAGEN) or Phenol-Chloroform extraction. 250-500ng DNA was bisulfite converted with the EZ DNA Methylation-Lightning Kit (Zymo Research) according to manufacturer instructions. Converted DNA was eluted twice in 10 µl elution buffer. Bisulfite PCR primer sequences provided in Supplementary Table 6. Products were amplified

using FastStart PCR Master Mix (Roche), purified using the QIAquick PCR purification Kit (QIAGEN) and subcloned into pGEMT-easy (Promega). Individual bacterial colonies were sanger sequenced using M13 sequencing primers, analysed using BISMA⁶⁷ and results formatted with the BiQ Analyzer Diagrams tool⁶⁸. In two independent experiments of NPC/EB differentiation, the following cell lines were used: For EB experiments: WT3, hom2 (n=2); WT1, hom3, het (n=1). For NPC, WT1, hom2, hom3, het (n=2); WT2, WT3, hom1 (n=1).

Reduced Representation Bisulfite Sequencing (RRBS)

Genomic DNA isolated with DNeasy Blood & Tissue Kit (QIAGEN) or Nucleon BACC2 Genomic DNA Extraction Kit (illustra) and quantified by Qubit (Invitrogen). DNA from mouse cortex samples were concentrated using Agencourt AMPure XP technology. 200ng of purified DNA samples (for NPC differentiation: DNA from experiment depicted in Fig.5c; for mouse cortexes in Fig. 6d, Supplementary Fig. 9e) were processed using the Ovation RRBS Methyl-Seq system kit (NuGen Technologies) according to instructions with modifications documented in the Supplementary Note. RRBS sequencing was aligned and processed using Bismark (v0.16.3)⁶⁹.

Processed RRBS files were assessed for conversion efficiency based on the proportion of methylated reads mapping to the λ genome spike-in (>99.5% in all cases, Supplementary Table 9) and processed in R to call DMRs. Alignment statistics provided in Supplementary Table 9. BigWigs were generated from RRBS data using CpGs with coverage ≥ 5 . BigWigs for Patient 3 and Control 3 were generated only from CpGs with coverage ≥ 5 in both samples to facilitate visual

comparison (shown Figure S3d). Overall summaries of RRBS data are shown in Figure S10c, f-h. Mean methylation in each sample was calculated as the weighted mean across all CpGs observed on autosomes irrespective of coverage (methylated coverage/total coverage).

Generation of Dnmt3a^{W326R} mice

A template for *in vitro* transcription was prepared by PCR, using the pX458-based plasmid containing the Dnmt3a-targeting gRNA sequence, a T7-tagged gRNA specific forward primer and a universal reverse primer (sequences Supplementary Table 6), PCR product purified by QIAquick PCR Purification (QIAGEN) and gRNA was produced by *in vitro* transcription (NEB HiScribe T7 High Yield RNA Synthesis Kit) using 1 µg of PCR product, and purified using the RNeasy Mini Kit (QIAGEN). Transgenic mice were generated by cytoplasmic injection of gRNA (25 ng/µl), Cas9 mRNA (50 ng/µl; L-6125; TriLink Biotechnologies) and ssODN repair template (150 ng/µl) into B6CBAF1/J single cell embryos. All resulting pups were screened by PCR amplification and sanger sequencing of the targeted region (primer sequences, Supplementary Table 6). F0 males were crossed with CD-1 females to establish germline transmission. F1 Dnmt3a^{W326R/+} males were crossed with CD-1 females and F2 offspring used for phenotyping and tissue collection (investigators were blinded to genotypes). Mouse studies were approved by the University of Edinburgh animal welfare and ethical review board (AWERB) and conducted according to UK Home Office regulations under a UK Home Office project license.

Statistical analysis

Statistical testing was performed using *R* v3.4.2 and GraphPad PRISM 6. Tests used indicated in figure legends. All tests were two-sided, unless otherwise stated. Further details of specific analyses provided in the relevant methods sections, below and Supplementary Note.

Hierarchical clustering

Clustering was performed on processed Infinium Beta probe values using *R* (Pearson correlation distance and Ward method). Cluster significance was tested using the CRAN package '*pvclust*' (v2.0.0).

Differentially methylated region identification

Windows of 5 contiguous probes or CpGs were used to identify DMRs for Infinium and RRBS data respectively. For Infinium arrays DMRs were called on the basis of ≥ 3 probes in a window having a difference in Beta value of at least 0.1 between each individual patient sample and each of the two control fibroblast lines, changed in the same direction, and with no CpG ≥ 1000 bp from its neighbours in the window. For this analysis we also only considered probes showing the same difference in both the patient 1 replicates. Overlapping or contiguous DMR windows were merged. For enrichment analyses, the set of DMR probes was compared to a genome-wide background control set of 'All' probes, derived from genomic regions spanning genomically-contiguous probes that fulfilled the same distance threshold criteria (ie. CpG ≤ 1000 bp from neighbours). DMR methylation level, defined as the mean Beta value of all probes located in the DMR. Fibroblast DMRs are provided in Supplementary Tables 2 and 3.

For RRBS data DMRs were called using a binomial linear model to test for a difference in the proportion of methylated reads for each CpG in the homozygous mutant samples versus controls. CpGs showing significant differences were then identified as those with Benjami-Hochberg adjusted p-values <0.05. DMRs were then called in a manner similar to that used for the Infinium arrays but using a distance threshold of 200bp. A control set of CpG sites that were within the distance threshold was used as a background control set of 'All' CpGs for enrichment analyses. Only CpGs where coverage was ≥ 10 in all samples were considered for DMR calling (1,516,046 CpGs). For RRBS DMR methylation level was defined as the weighted mean methylation level (methylated coverage/total coverage) from all CpGs observed within the DMR region irrespective of coverage. NPC DMRs are provided in Supplementary Tables 5 and 10.

Enrichment of DMRs in ChromHMM segmentations

Infinium probes were mapped to existing ChromHMM annotations⁷⁰ using the *BEDtools intersect* function (v2.27.1)⁷¹. Identical ChromHMM labels were merged for analysis. To test for enrichment of an annotation, a Fisher's exact test was performed for number of DMR probes against number of control probes.

DNA methylation valley analysis

Previously reported DMVs²⁶ were mapped to hg19 using the UCSC *liftover* tool and merged DMV regions from all 5 cell-types determined using the *Bedtools merge* function. DMV methylation level, defined as mean Beta value of all probes present in the DMV. DMVs were then mapped to their closest genes using ChIPpeakAnno

(details Supplementary Note). Using DMR and control gene lists (as defined in GO analysis section), DMR enrichment at DMVs was tested by Fisher's exact test, comparing the proportion of DMR-associated genes that were DMV genes with the proportion of control genes that were DMV genes.

Analysis of histone modifications at DMRs, DMVs and ChIP-seq peaks

Non-overlapping windows of 250bp (for DMRs and ChIP-seq peaks) or 500bp (for DMVs) were defined centred on each region of interest, with ChIP-seq read counts/window calculated using BEDtools' *coverage* function. Read counts were scaled to counts per 10 million based on total number of mapped reads/sample and divided by the input read count to provide a normalised read counts. To prevent windows with zero reads in the input sample generating a normalised count of infinity, an offset of 0.5 was added all windows prior to scaling and input normalisation. Regions where coverage was 0 in all samples were removed from the analysis. ChIP-Rx was analysed similarly before samples were scaled using a normalisation factor generated from the number of reads mapping to the spike-in *Drosophila* genome. Reads mapping to the *Drosophila* genome in each ChIP and input sample were first scaled to reads per 1×10^7 . The scaling factor was then calculated as the ratio of the scaled *Drosophila* reads in two ChIP samples over their respective ratio from the input samples, ie scaling factor, S , for sample n compared to reference sample ref : $S_n = (dRPTM_{ChIP-n} / dRPTM_{ChIP-ref}) / (dRPTM_{IN-n} / dRPTM_{IN-ref})$, where $dRPTM$ = *Drosophila* Reads per 1×10^7 for *ChIP* and input, *IN*, runs respectively (modified from published method to take account of the presence of an input sample)⁶⁵. To statistically test differences in histone modification levels, normalised read depths across DMRs/DMVs were compared using a Wilcoxon rank

sum test. H3K27me3-marked DMVs defined as those containing a H3K27me3 ChIP-seq peak replicated in both control fibroblast lines. H3K27me3 and H3K4me3 peaks used for quantitative analysis were defined by merging peaks called in the two controls (using *Bedtools merge*). Only autosomal peaks overlapping those called in both control samples and containing Infinium probes in the background control set from DMR calling were used for analysis. The subsets of these peaks overlapping DMRs were defined using *Bedtools intersect*. The change in histone modification levels within regions of interest was defined as the \log_2 ratio of the mean mutant normalised read count over control normalised read count. The profile of H3K36me3 at DMVs was generated by calculating normalised read counts in 10 scaled windows across DMVs together with 500bp windows extending 10Kb up- and down-stream of each DMV. Colour scales for ChIP-seq heatmaps range from the minimum to the 90% quantile of the normalised read count for the reference dataset in each set of heatmaps.

Analysis of enrichment of histone modifications at DMRs

BEDtools intersect was used to overlap DMR probes with histone modification peaks. % DMR probes mapping to peaks was tested against % background control probes mapping to peaks using a Fishers exact test. A similar strategy was applied for mouse RRBS DMRs, testing DMR CpG versus background control CpG sites.

RNAseq analysis

To analyse RNAseq, the number of reads mapping to each ENSEMBL annotated gene (human: *Release 75/GCRh37*, mouse: *Release 91/mm10*) was calculated using the *featureCounts* module of the *subread* aligner (v1.5.2)⁷². Only reads

mapping to exons were considered. Gene read counts were then analysed using *EdgeR* (v3.18.1)⁷³ with Trimmed Mean of M-values (TMM) normalization⁷⁴. The log₂ normalised counts per million (CPM) and log₂ ratios calculated by *EdgeR* were then subject to further analysis. Only genes where CPM was >1 in ≥2 samples and that are annotated as protein coding in ENSEMBL were considered for analysis (human fibroblasts, 11,963 genes; mouse NPCs, 13,022 genes). To generate lists of genes differentially regulated in published data of mES cells differentiated to terminally differentiated neurons³⁸, similar pre-processing was applied (resulting in data for 14,780 genes). Differential expression was then called using an F-test of a generalised linear model fitted to the data taking account of sample batch using *EdgeR*. Up and down regulated genes were called as those with Benjamini-Hochberg corrected FDR < 0.01 and a log-fold change >|1| (4,147 and 4,067 genes respectively). Genes unchanged in the analysis were defined as those with Benjamini-Hochberg corrected FDR > 0.05 (4,067 genes).

Reporting Summary

Further information on experimental design is available in the Reporting Summary.

Data availability

The human next-generation sequencing data used in the manuscript are available on request from the relevant Data Access Committee from the European Genome-Phenome Archive (EGA). The exome data is available under the accession EGAS00001003231. Human RNA-seq, RRBS and ChIP-seq under the accession EGAS00001003232. The data are not publicly available to ensure protection of patient sequence data confidentiality through controlled access. Processed data files

1024 and mouse RNA-seq/RRBS are available in GEO under accession (awaiting
1025 accession number).

1026

1027

1028

1029 **Methods only**

1030

1031

1032

1033

1034

1035

1036

1037

1038

1039

1040

1041

1042

1043

1044

1045

1046

1047

1048

1049

1050

1051

1052

1053

1054

1055

1056

1057

1058

1059

1060

1061

1062

1063

1064

1065

1066

1067

1068

1069

1070

1071

1072

1073

1074

1075
1076
1077
1078
1079
1080
1081
1082
1083
1084
1085
1086

references:

1087
1088
1089
1090
1091
1092
1093
1094
1095
1096
1097
1098
1099
1100
1101
1102
1103
1104
1105
1106
1107
1108
1109
1110
1111
1112
1113
1114
1115
1116
1117
1118
1119

58. Barski, A. *et al.* High-resolution profiling of histone methylations in the human genome. *Cell* **129**, 823-37 (2007).
59. Murray, J.E. *et al.* Extreme growth failure is a common presentation of ligase IV deficiency. *Hum Mutat* **35**, 76-85 (2014).
60. de Bruin, C. *et al.* An XRCC4 splice mutation associated with severe short stature, gonadal failure, and early-onset metabolic syndrome. *J Clin Endocrinol Metab* **100**, E789-98 (2015).
61. Guerois, R., Nielsen, J.E. & Serrano, L. Predicting changes in the stability of proteins and protein complexes: a study of more than 1000 mutations. *J Mol Biol* **320**, 369-87 (2002).
62. Triche, T.J., Jr., Weisenberger, D.J., Van Den Berg, D., Laird, P.W. & Siegmund, K.D. Low-level processing of Illumina Infinium DNA Methylation BeadArrays. *Nucleic Acids Res* **41**, e90 (2013).
63. Fortin, J.P., Triche, T.J., Jr. & Hansen, K.D. Preprocessing, normalization and integration of the Illumina HumanMethylationEPIC array with minfi. *Bioinformatics* **33**, 558-560 (2017).
64. Illingworth, R.S., Holzspies, J.J., Roske, F.V., Bickmore, W.A. & Brickman, J.M. Polycomb enables primitive endoderm lineage priming in embryonic stem cells. *Elife* **5**(2016).
65. Orlando, D.A. *et al.* Quantitative ChIP-Seq normalization reveals global modulation of the epigenome. *Cell Rep* **9**, 1163-70 (2014).
66. Tarasov, A., Vilella, A.J., Cuppen, E., Nijman, I.J. & Prins, P. Sambamba: fast processing of NGS alignment formats. *Bioinformatics* **31**, 2032-4 (2015).
67. Rohde, C., Zhang, Y., Reinhardt, R. & Jeltsch, A. BISMA--fast and accurate bisulfite sequencing data analysis of individual clones from unique and repetitive sequences. *BMC Bioinformatics* **11**, 230 (2010).
68. Bock, C. *et al.* BiQ Analyzer: visualization and quality control for DNA methylation data from bisulfite sequencing. *Bioinformatics* **21**, 4067-8 (2005).
69. Krueger, F. & Andrews, S.R. Bismark: a flexible aligner and methylation caller for Bisulfite-Seq applications. *Bioinformatics* **27**, 1571-2 (2011).
70. Ernst, J. & Kellis, M. ChromHMM: automating chromatin-state discovery and characterization. *Nat Methods* **9**, 215-6 (2012).

- 1120 71. Quinlan, A.R. & Hall, I.M. BEDTools: a flexible suite of utilities for comparing genomic
1121 features. *Bioinformatics* **26**, 841-2 (2010).
1122 72. Liao, Y., Smyth, G.K. & Shi, W. featureCounts: an efficient general purpose program
1123 for assigning sequence reads to genomic features. *Bioinformatics* **30**, 923-30 (2014).
1124 73. Robinson, M.D., McCarthy, D.J. & Smyth, G.K. edgeR: a Bioconductor package for
1125 differential expression analysis of digital gene expression data. *Bioinformatics* **26**,
1126 139-40 (2010).
1127 74. Robinson, M.D. & Oshlack, A. A scaling normalization method for differential
1128 expression analysis of RNA-seq data. *Genome Biol* **11**, R25 (2010).
1129

1130

Figure 1

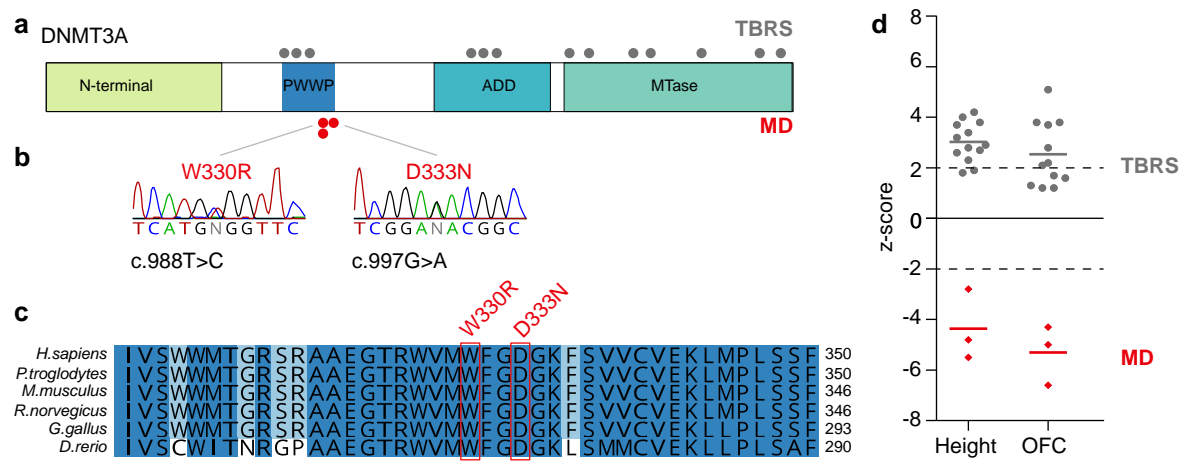


Figure 2

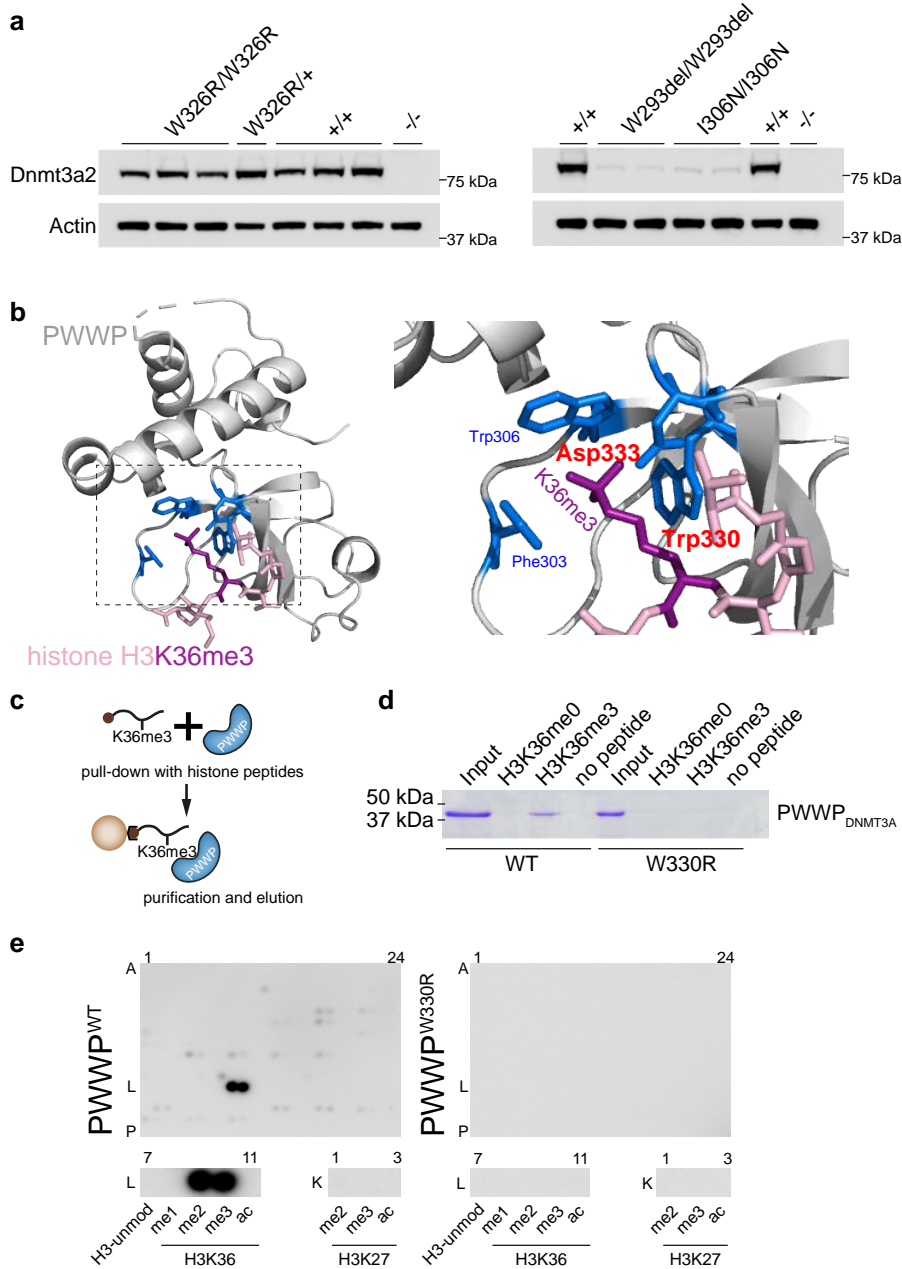


Figure 3

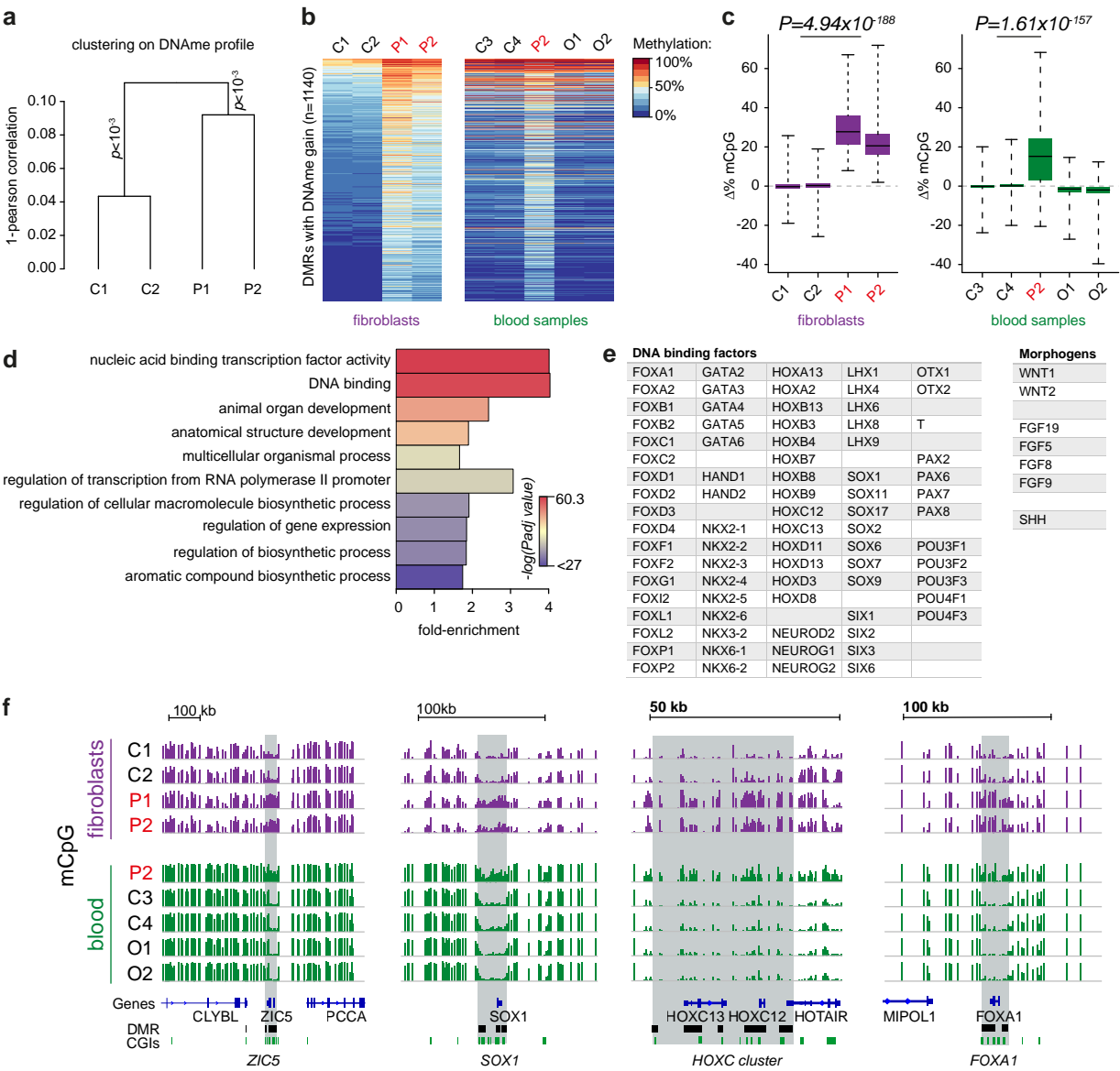


Figure 4

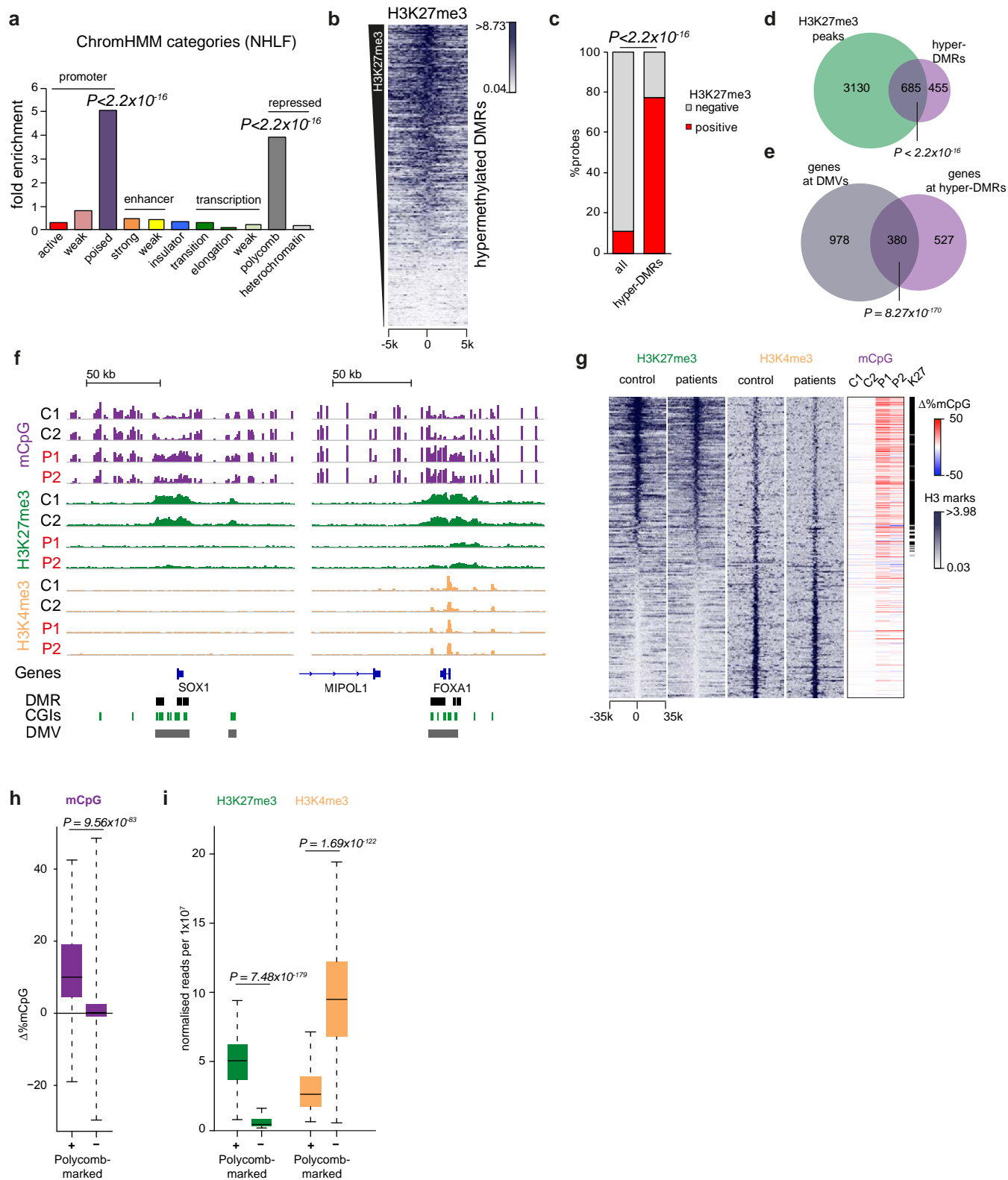


Figure 5

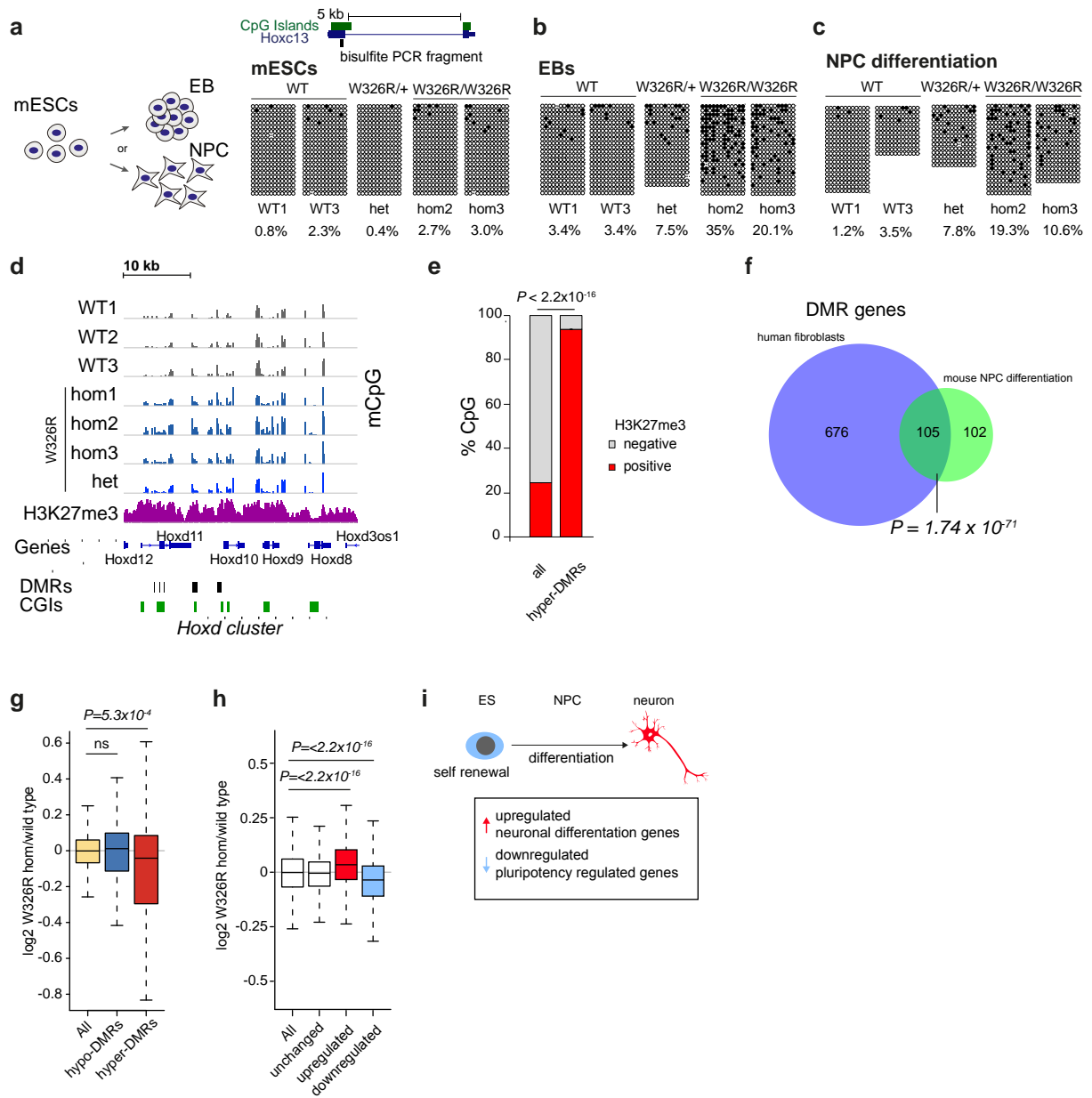


Figure 6

